Volume 4
Number 11
November 2025
Pages 919–1038

Sensors & Diagnostics

rsc.li/sensors

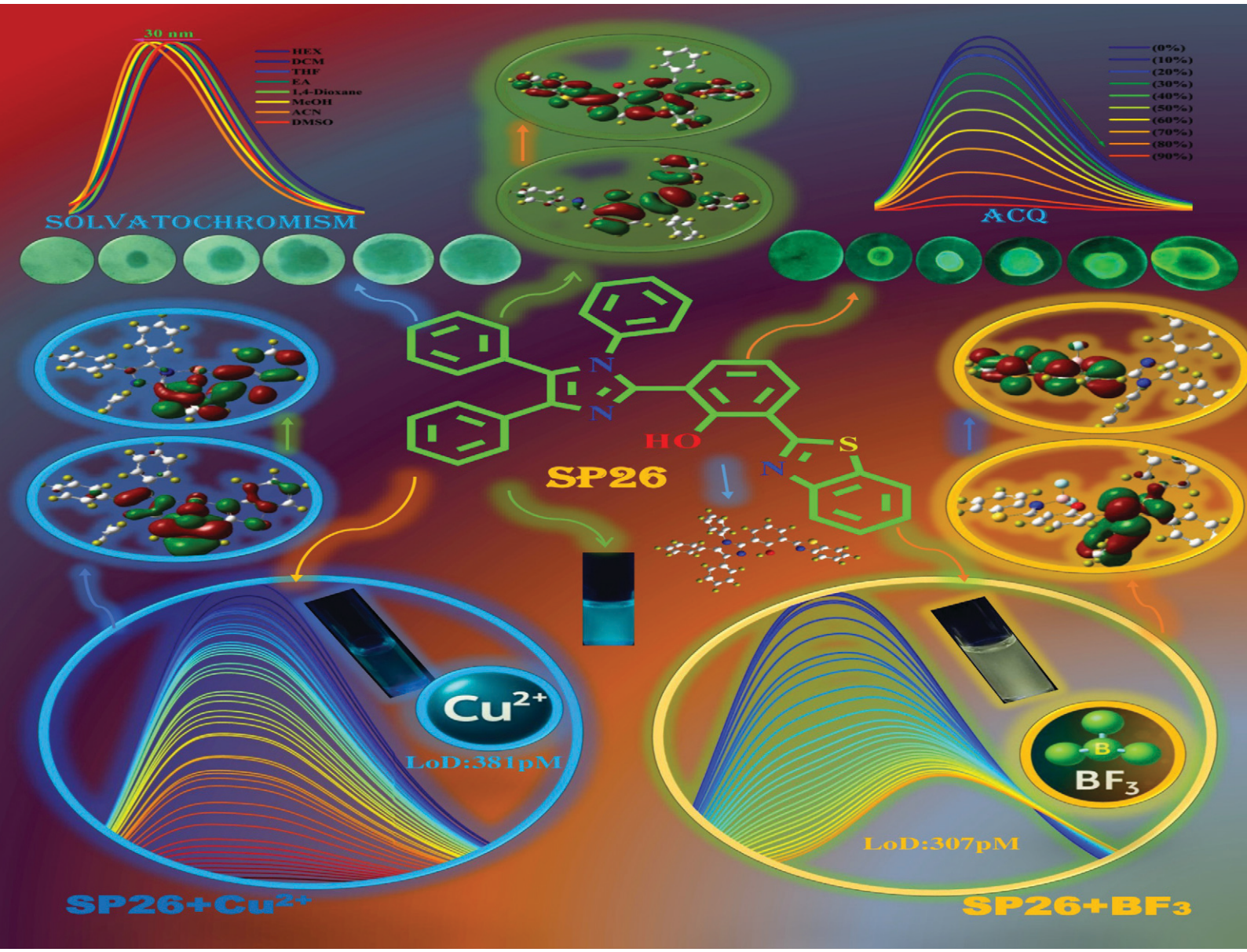

ISSN 2635-0998

ROYAL SOCIETY OF CHEMISTRY

PAPER

Prakash Seenu and Sathiyanarayanan Kulathu Iyer
An imidazole-based fluorescent sensor for selective detection of Cu^{2+} and BF_3 with environmental applications

Sensors & Diagnostics

PAPER

View Article Online
View Journal | View Issue

Cite this: *Sens. Diagn.*, 2025, **4**, 973

An imidazole-based fluorescent sensor for selective detection of Cu^{2+} and BF_3 with environmental applications

Prakash Seenu and Sathiyanarayanan Kulathu Iyer *

The specific detection of Cu^{2+} and BF_3 provided the basis for the design of the distinctive dual-sensing chemosensor, 2-(benzo[*d*]thiazol-2-yl)-6-(1,4,5-triphenyl-1*H*-imidazol-2-yl) phenol (**SP26**). **SP26** was synthesized successfully using a multi-step process, with its identity confirmed by NMR spectroscopy and HR-MS analysis. The studies were conducted in an 8 : 2 THF/water mixture. The ligand was solubilized in THF/water, whereas the cation salts were dissolved in water. The absorption measurements indicated no detection of cations other than Cu^{2+}. The emission experiments revealed that the optical selectivity for the Cu^{2+} ion leads to a reduction in emission intensity. Likewise, with BF_3, the emission intensity diminishes with the bathochromic shift. The limit of detection (LoD) for Cu^{2+} is 381 pM, and for BF_3 it is 307 pM. After adding BF_3 and Cu^{2+} to **SP26**, the complex formation was so quick that it happened within a fraction of a second. Triethylamine (TEA) was used for BF_3, and ethylenediamine tetraacetic acid (EDTA) for Cu^{2+} to determine the reversibility. FT-IR, HR-MS, Job's plot, DFT, and ^1H NMR titration analyses confirmed that chemosensor **SP26** was bound to Cu^{2+} and BF_3. Paper test strips showed the potential of the chemosensor **SP26** for the environmental detection of Cu^{2+} and BF_3. The quantitative analysis of Cu^{2+} was examined with environmental water samples.

Received 13th February 2025,
Accepted 29th August 2025

DOI: 10.1039/d5sd00021a

rsc.li/sensors

1. Introduction

Copper is one of the most prevalent transition metal ions in the human body due to its important applications in biology, chemistry, and the environment, and it has garnered much attention. It is essential for haemopoiesis and other processes catalyzed by proteins and enzymes. While Cu^{2+} is necessary for human health, an excess of it can tilt the delicate balance within cellular functions and leads to severe neurodegenerative illnesses, including Parkinson's, Wilson's, and Alzheimer's diseases, and similar conditions.[1,2] Furthermore, Cu^{2+} is widely used in industry and daily life, even though it is considered a significant metal pollutant. Thus, creating straightforward, effective, sensitive, and precise techniques for Cu^{2+} detection is imperative.

Numerous methods have been developed in the last few decades for the detection of Cu^{2+}, including electrochemical methods,[3,4] atomic absorption spectrometry (AAS),[5,6] inductively coupled plasma-atomic emission spectrometry (ICP-AES),[7,8] inductively coupled plasma mass spectroscopy (ICPMS),[9] and emission methods.[10–15] Fluorescent probes have emerged as one of the most effective tools for detecting metal ions and other pollutants because of their many exceptional benefits, including simplicity, ease of manipulation, great sensitivity and selectivity, and real-time detection. Notwithstanding, most documented emission probes for Cu^{2+} detection utilize emission quenching or augmentation,[16–19] in which the instrument, auto-emission, manipulation errors, and surroundings can be readily impacted.

They are unable to offer measures that are quantitatively accurate enough. The current probe is capable of detecting a very low level of Cu^{2+} (381 pM). However, ratiometric chemosensor probes for Cu^{2+} detection are still uncommon as of right now. Cu^{2+} ions are also harmful to marine plants such as algae.[20] These things make the detection of Cu^{2+} ions indispensable and immediately warranted. The synthesis and application of a good fluorescent sensor should be straightforward, as on-site chemical information can be easily obtained. The design of a fluorescent sensor is the art of clubbing the points of attachment with the fluorophore. In the case of Cu^{2+} ion detection sensors containing quinoline,[21–23] naphthalimide,[24,25] rhodamine,[26,27] and pyrene,[28] development has been achieved. However, the stability and ease of synthesis are the major stumbling blocks for these sensors.

The important inorganic compound boron trifluoride (BF_3) is frequently employed as a catalyst in various organic synthesis processes,[29] including condensation, ionic polymerization, and isomerization.[30] However, BF_3 is extremely poisonous and

Department of Chemistry, School of Advanced Sciences, Vellore Institute of Technology, Vellore-632014, India. E-mail: sathiyanarayanank@vit.ac.in

corrosive, and even small leaks can result in biological dangers and other environmental problems. Moreover, BF_3 has a very high reactivity and can react violently with metals, organic materials, *etc.* BF_3 will produce a powerful explosion and break down into HF, which can irritate the nose, eyes, skin, respiratory tract, or even cause death, especially when it comes into contact with water or even humid air.[31] In summary, BF_3 is a hazardous gas that must be handled carefully during application, transportation, production, and disposal activities. Dependable gas leak detection systems for BF_3 are now vitally needed to provide a safe working environment and reduce production loss.[32]

The chemisorption of BF_3 and its monohydrate with a gas-reactive thin film placed on a slice of quartz served as the basis for the construction of the quartz microbalance (QMB) sensor technology. They have the following shortcomings, which should be noted: complicated instruments, lengthy response times, high detection limits, and operating procedures. Thus, the benefits of the fluorescence sensing approach, which include easy operation, high sensitivity, fast response, and field test availability, have led to its widespread application in recent years.[33] T.-H. Tran-Thi and colleagues[33] in 2008 demonstrated a hybrid mesoporous organo-silica functionalized with grafted dibenzoylmethane (DBM) exhibiting fluorescence that can be enhanced in the presence of BF_3 over a few hours at a low sensitivity concentration (<1 ppm) to break the Et_2O–BF_3 complex and permit BF_3 to diffuse and react with DBM. A novel molecular design for sensing BF_3 was used by Eric T. Kool *et al.* in 2011. DNA-polyfluorophores may produce distinct selective responses at concentrations as low as 20 ppm when seen under an epifluorescence microscope.[34] This system offers straightforward operation, fast response time, and *in situ* detection, and it does not require large-scale sensors as previous approaches did. However, the sensitivity of this approach exceeds the permissible exposure limit (PEL) and threshold limit value (TLV) of 1 ppm set by the Occupational Safety and Health Administration (OSHA) and the American Conference of Governmental Industrial Hygienists (ACGIH).

Imidazole-based fluorescent sensors were studied. However, they have some disadvantages, like some imidazole sensors' limited solubility. Imidazole possesses a nitrogen donor capable of coordinating with several metal ions (*e.g.*, Cu^{2+}, Zn^{2+}, Fe^{3+}), making the differentiation between analogous ions challenging.

An imidazole sensor ensures precision and dependability in selective detection. Certain imidazole-based sensors demonstrate sluggish reaction times or irreversible interactions with the target, rendering them inadequate for real-time or dynamic monitoring.

For example, a highly fluorescent imidazole-based diboron complex has been synthesized, and only photophysical studies were carried out.[35] Similarly, imidazoyl-phenol-based boron complexes have been studied extensively.[36] Cu^{2+} sensing and electrochemical removal were done using triphenyl-imidazole-based sensors.[37] A novel imidazole-derived chemosensor was developed for the detection of Cu^{2+} and sulphide ions.[38] Similarly, a bifunctional chemosensor for the detection of Cu^{2+} and Fe^{2+} was developed using push–pull imidazole–triazole.[39] However, an imidazole-derived Schiff base was used for the identification of Cu^{2+} and applied in fingerprint images from our laboratory.[40] Similarly, from our laboratory, an imidazole-tethered benzothiazole sensor was developed for the detection of picric acid and latent fingerprint images.[41]

To effectively synthesize fluorescent chemosensors for the recognition of both Cu^{2+} and BF_3, we have established a new chemical technique for the synthesis through the cyclocondensation reaction yielding **2-(benzo[*d*]thiazol-2-yl)-6-(1,4,5-triphenyl-1*H*-imidazol-2-yl) phenol (SP26)**. To address this, we have created the small-molecule chemosensor **SP26**, which interacts with Cu^{2+} and BF_3 by deprotonation. **SP26** has outstanding selectivity, sensitivity, and optical responsiveness due to multiple points of attachment (N, O, N) to the sensor.

Furthermore, the chemosensor **SP26** has robust electron-donating characteristics that facilitate energy induction and electron transfer and facilitate fluorescence quenching through fluorophore–analyte interactions. For Cu^{2+} and BF_3 in test strips, **SP26** was used to demonstrate practical applicability. Therefore, the information from this work will be useful in designing more sophisticated fluorescent chemosensors for precise and targeted detection at very low concentrations.

1.1 General

All the chemicals used in this investigation, including solvents like ethanol and tetrahydrofuran (THF), were of analytical reagent (AR) grade. $B(OMe)_3$, borax, BPh_3, H_3BO_3, BCl_3, $NaBF_4$, H_2S, $HClO_4$, NaF, HCl, NaCN, N_2H_4, NH_3, and NH_4Cl, and the metal salts containing Ag^+, Al^{3+}, Ba^{2+}, Ca^{2+}, Cr^{3+}, Cd^{2+}, Cu^{2+}, Co^{2+}, Hg^{2+}, Ni^{2+}, Zn^{2+}, Zr^{2+}, and Th^{4+}, were obtained from Sigma Aldrich and Spectrochem and were used without any additional purification. The supplier of boron trifluoride diethyl etherate ($C_4H_{10}BF_3O$) was Avra Chemicals. Nuclear Magnetic Resonance (NMR) spectra, comprising ^1H and ^{13}C, were acquired using Bruker Avance III 400 MHz and 100 MHz. A JASCO FP-8655 fluorophotometer was used for fluorescence spectroscopy. The instrument utilized for UV-visible spectroscopy was a JV-750. Column chromatography, which combines stationary (silica gel) and mobile (ethyl acetate-hexane) phases, was used to purify reaction mixtures.

1.2 Synthesis and characterisation

A solution of salicylaldehyde (1.5 g, 12.3 mmol) and 2-aminothiophenol (1.25 mL, 11.9 mmol) in EtOH (25 mL) was mixed dropwise with aq. HCl (37%, 30 mmol) and aq. H_2O_2 (30%, 48.0 mmol). We refluxed the mixture for one hour. After the reaction mixture attained room temperature, we filtered it and was given an ethanol wash followed by air drying. We obtained 1.4 g of pure white solid **2-(2-hydroxyphenyl) benzothiazole (HBA)** with a yield of 82%. Hexamethylenetetramine (HMTA) (0.926 g, 6.6 mmol) was mixed into a solution of **HBA** (1 g, 5 mmol) in CH_3COOH (20 mL) and refluxed for 3 hours. The reaction mixture was cooled to room temperature. Then, the reaction mixture was quenched in cold

water, pH-neutralized, filtered, and dried. Then, the precipitate was purified by column chromatography using silica gel 100–200 mesh and using ethyl acetate : *n*-hexane (1 : 9) as a solvent system, yielding 420 mg (45%). The solid of **3-(benzothiazole-2-yl)-2-hydroxybenzaldehyde (HBAA)** is light-yellow colored.[42]

Synthesis of 2-(benzo[*d*]thiazol-2-yl)-6-(1,4,5-triphenyl-1*H*-imidazol-2-yl) phenol (SP26) through cyclocondensation. 3-(Benzo[*d*]thiazol-2-yl)-2-hydroxybenzaldehyde 0.300 g (1 equivalent), benzil 0.240 g (1 equivalent), and 0.1 mL (1 equivalent) of aniline were all dissolved in glacial acetic acid[43] and refluxed for 3 hours. The reaction's progress was seen using TLC with ethyl acetate : *n*-hexane (3 : 7). After the reaction's completion, the reaction mixture was cooled to room temperature, and cold water was added. After that, sodium hydroxide solution was added to neutralize the reaction mixture. The solid was separated and allowed to air dry. For purification, the reaction mixture was separated and purified using column chromatography with a silica gel mesh size of 100–200 and ethyl acetate : *n*-hexane as the eluent. In the end, a solid light-yellow compound with a yield of 76% was achieved. The compound purity was 99.20% (Fig. S3). High-resolution mass spectrometry and NMR spectroscopy were used to analyze the molecule (M. P.: 237 °C). The estimated mass of the compound was 521.1628, while its observed mass with the proton adduct was 522.1636 (Fig. S4). ^{1}H NMR (400 MHz, DMSO) δ: 11.835 (s) (1H), 8.305–8.299 (d) 2.4 Hz (1H), 8.143–8.123 (d) 8 Hz (1H), 8.060–8.041 (d) 7.6 Hz (1H), 7.196–7.551 (m) (18H), 6.988–6.966 (d) 8.8 Hz (1H) SI (Fig. S1). ^{13}C NMR (100 MHz, DMSO) δ: 164.81, 156.73, 156.65, 151.86, 156.81, 145.87, 134.90, 134.77, 132.42, 131.78, 131.60, 131.50, 130.90, 130.13, 129.79, 129.34, 129.24, 129.15, 129.09, 129.05, 128.94, 128.85, 128.66, 126.87, 126.57, 125.68, 122.78, 122.69, 121.51, 122.42, 118.62, 117.22 SI (Fig. S2) (Scheme 1).

1.3 Stock solution preparation

Metal nitrate salts were dissolved in double-distilled water to yield solutions with a concentration of 1×10^{-3} M. Meanwhile, a 2×10^{-5} M stock solution of the chemosensor (**SP26**) was prepared using tetrahydrofuran–water (8 : 2-THF : H_2O) as the solvent before conducting every photophysical study, and the excitation wavelength is 360 nm for all photophysical studies.

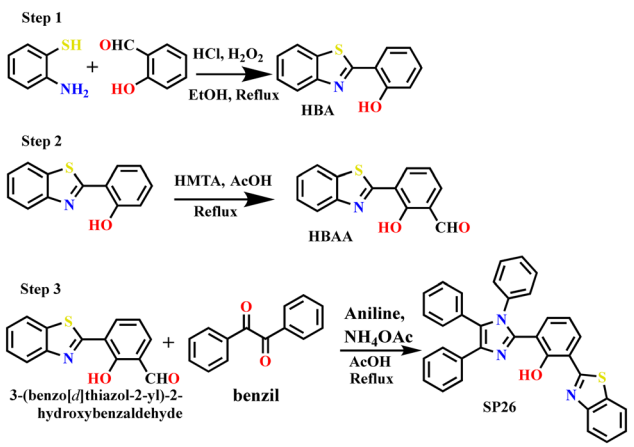

Scheme 1 The synthesis of 2-(benzo[*d*]thiazol-2-yl)-6-(1,4,5-triphenyl-1*H*-imidazol-2-yl) phenol (**SP26**).

2. Results and discussion

2.1 Absorption studies at different H_2O–THF combinations

SP26 produces a green color in solution when dissolved in THF. After that, several combinations of THF/water fraction of 0–90% were created; the absorption spectrum was recorded with each solution; there are two peaks at 300 and 360 nm, and there is a slight decrease at 300 nm in the absorption up to 70% of water. At 80% and 90% of water, there is a sudden increase in absorption (Fig. 1a).

2.2 Aggregation caused quenching (ACQ) of emission

Similar to the absorption spectrum, the emission spectrum was recorded, and there is a considerable reduction in the emission intensity as we increase the water content of the solvent system. The FL spectrum shows that emission intensity is gradually decreasing up to 50% of water. After 60% of water, the emission disappeared as the water was added, due to the aggregation-caused quenching (ACQ) effect (Fig. 1b). It is shown in the form of a bar chart with different water fractions, under 365 nm UV light, as seen in Fig. 1c. In this particular study, the ACQ may help the detection of Cu^{2+}, since the addition of Cu^{2+} leads to quenching.

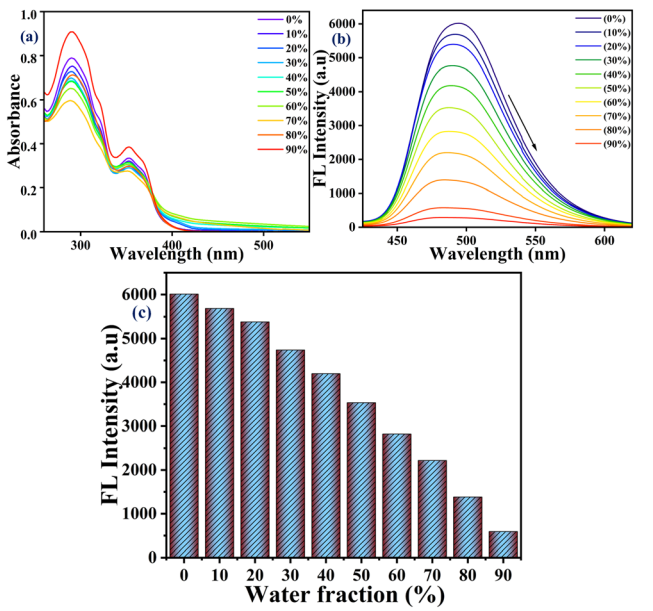

Fig. 1 (a) Absorption spectra of **SP26** in various combinations of THF/water. (b) Emission spectra of **SP26** in various combinations of THF/water; the excitation wavelength is at 360 nm and the emission wavelength is at 500 nm, and the scanned wavelength is 400 to 650 nm at room temperature. (c) The bar graph of **SP26** at various combinations of THF/water under 365 nm UV light.

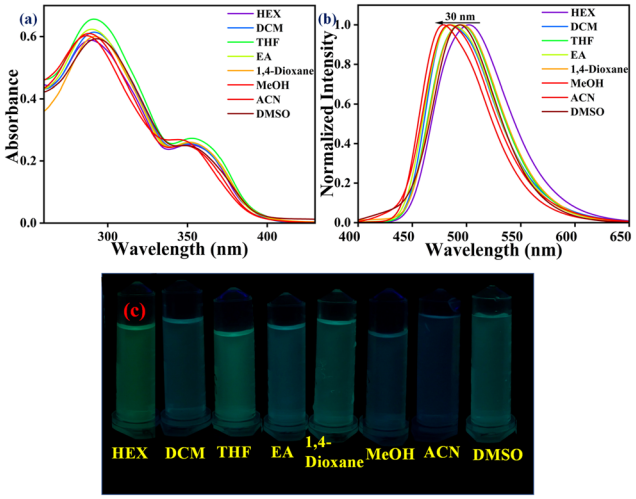

Fig. 2 (a) Absorption spectra of **SP26** in various solvents (solvatochromism). (b) Emission spectra of **SP26** in various solvents (solvatochromism); the excitation wavelength is at 360 nm and the emission wavelength is at 500 nm, and the scanned wavelength is 400 to 650 nm at room temperature. (c) Colours of **SP26** in various solvents under 365 nm UV light.

2.3 Solvatochromism properties

The absorption and emission spectra of compound **SP26** in different solvents, such as *n*-hexane (HEX), dichloromethane (DCM), tetrahydrofuran (THF), ethyl acetate (EA), 1,4-dioxane, methanol (MeOH), acetonitrile (ACN) and dimethyl sulfoxide (DMSO), show a broad signal as shown in Fig. 2(a) and (b). The photophysical properties of the compound are summarized in Table 1 in various solvents. The sensitivity of the absorption spectrum is weak because the local environment of the molecules in the ground and excited states remains unchanged during the fast absorption process, and there is not much difference. On the other hand, a blue shift to 30 nm was observed in the emission spectra in different solvents when the solvent system's polarity was increased from hexane to DMSO. As a result, it displays negative solvatochromism, which shifts from the longer wavelength to the shorter wavelength as polarity increases. This shows that the ground state is more stabilised than the excited state due to a large energy gap.[44,45] The interaction between the dipoles of the solvent and ligand makes the ligand unstable in the excited state, leading to a very high energy state. This was evident from the difference between the HOMO and LUMO of the ligand from theoretical calculations.

2.4 Selectivity studies

In the presence of several boron species and metal ions (BF_3, $B(OMe)_3$, borax, BPh_3, H_3BO_3, BCl_3, $NaBF_4$, H_2S, $HClO_4$, NaF, HCl, NaCN, N_2H_4, NH_3, and NH_4Cl, Ag^+, Al^{3+}, Ba^{2+}, Ca^{2+}, Cr^{3+}, Cd^{2+}, Cu^{2+}, Co^{2+}, Hg^{2+}, Ni^{2+}, Zn^{2+}, Zr^{2+}, and Th^{4+}), the UV-vis absorption and emission studies were conducted on **SP26** in 2×10^{-5} M concentration in a solvent ratio of 8 : 2 tetrahydrofuran : water (THF : H_2O). Two absorption bands at 300 nm and 360 nm in the absorption spectrum of **SP26** are due to the π–π* and n–π* transitions, respectively. New absorption bands appeared after complexation with the addition of BF_3 and Cu^{2+}. When BF_3 was added gradually, the absorption band that had first emerged at 360 nm moved hypsochromically to 340 nm. The band at 360 nm disappears when we add Cu^{2+}, and a second, smaller absorption band at 400 nm appears, as seen in Fig. 3a. Thus, for fluorescence spectroscopic examination of the sensor **SP26**, the excitation wavelength was set at 360 nm. Similarly, the sensor gave an emission band at 500 nm. The sensor **SP26's** emission band was measured in the presence of Cu^{2+}, the emission band was quenched at 500 nm, and for BF_3, the emission band was quenched and gradually redshifted to 550 nm.

2.5 Absorption and emission titration studies

The π–π* transition of sensor **SP26** appears at 300 nm for the absorption; the n–π* transition is exhibited at 360 nm. Fig. 4a shows that the intensity of the absorption peak at 300 nm increases and a new peak at 400 nm increases progressively, and the peak at 360 nm decreases, when 0 to 3 equivalents of Cu^{2+} are added (Fig. 4a). Hence, we obtained an isosbestic point at 372 nm and there is a marked red shift in the absorption spectra. However, upon adding 0 to 2 equivalents of BF_3 to **SP26**, a new peak at 260 nm emerges at the expense of the peak at 300 nm. Unlike copper, in the case of BF_3, the absorption increases as the BF_3 concentration is increased, and also there is a clear blue shift. Another new absorption peak at 310 nm decreases till 320 nm, again it increases up to 362 nm, then it decreases. A regular

Table 1 Photophysical properties of **SP26** in different solvents at room temperature

Probe	Solvent[a]	λ_{max}[b] (nm)	log ε[c] (10^4 M^{-1} L^{-1} cm^{-1})	FWHM[d] (nm)	λ_{em}[e] (nm)	λ_s[f] (cm^{-1})	ϕ[g]
SP26	HEX	355	1.2	134.6	503	8289	0.0221
SP26	DCM	354	1.25	125	485	7630	0.0198
SP26	THF	351	1.35	126.4	495	8288	0.0181
SP26	EA	351	1.3	130.5	487	7957	0.0202
SP26	1,4-Dioxane	353	1.25	137.7	496	8167	0.0200
SP26	MeOH	348	1.3	132.4	486	8159	0.0252
SP26	ACN	351	1.2	132.4	479	7614	0.0220
SP26	DMSO	354	1.2	130.9	494	8006	0.0174

[a] Polar to non-polar solvents. [b] Maximum absorbance in UV-vis spectra. [c] Extinction coefficient. [d] Full-width at half maximum. [e] Wavelength of the maximum emission intensity. [f] Stokes shifts. [g] Quantum yield.

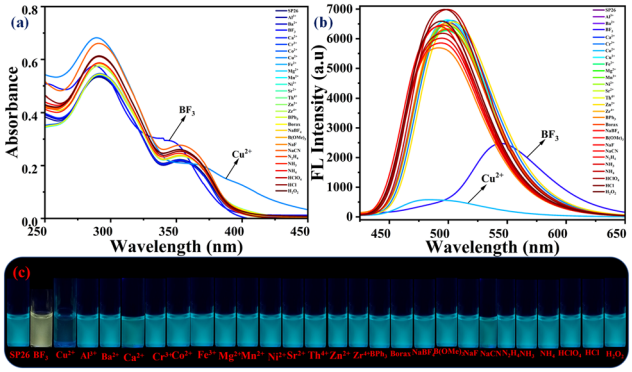

Fig. 3 (a) Absorption spectra of chemosensor **SP26** with different metal ions and different boron species in 8 : 2 THF : H_2O solution. (b) Emission spectra of chemosensor **SP26** with different metal ions and different boron species in 8 : 2 THF : H_2O solution; the excitation wavelength is at 360 nm and the emission wavelength is at 500 nm, and the scanned wavelength is 400 to 650 nm at room temperature. (c) Colours of **SP26** with different metal ions and boron species upon adding 1×10^{-3} M metal ions into 2×10^{-5} M concentrations of **SP26** in 8 : 2 THF : H_2O solution under 365 nm UV light.

blue shift was seen, unlike copper. As a result, we obtained three isosbestic points at 300, 320, and 362 nm upon adding BF_3. However, in the case of copper, we obtained only one isosbestic point. As a result, the shapes of the absorption spectra of Cu^{2+} and BF_3 are different. The complex formation between **SP26** and BF_3 was verified (Fig. 4b). Similarly, the fluorescence titration of **SP26** was performed by gradually adding Cu^{2+} (0 to 3 equivalents)

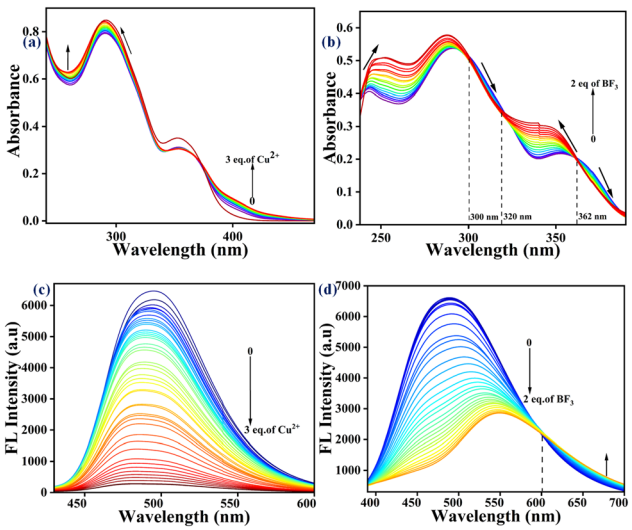

Fig. 4 (a) Absorption spectra of chemosensor **SP26** (2×10^{-5} M) in 8 : 2 THF : H_2O solution with 0–3 equivalents of Cu^{2+}. (b) Absorption spectra of chemosensor **SP26** (2×10^{-5} M) in 8 : 2 THF : H_2O solution with 0–2 equivalents of BF_3 analytes. (c) Emission spectra of chemosensor **SP26** (2×10^{-5} M) in 8 : 2 THF : H_2O solution with 0–3 equivalents of Cu^{2+}. (d) Emission spectra of chemosensor **SP26** (2×10^{-5} M) in 8 : 2 THF : H_2O solution with 0–2 equivalents of BF_3 analytes, and for both, the excitation wavelength is at 360 nm and the emission wavelength is at 500 nm, and the scanned wavelength is 400 to 650 nm at room temperature.

(Fig. 4c). When the concentration of Cu^{2+} increases, the **SP26** fluorescence band at 500 nm was quenched. Similarly, adding 0 to 2 equivalents of BF_3 resulted in a redshift towards 550 nm and diminished with an increase in BF_3 concentration. However, we also detected a second emission peak at 680 nm, which slightly increases as the BF_3 concentration rises. Hence, we obtained the isoemissive point at 600 nm (Fig. 4d). It is observed that fluorescence is quenched in the case of Cu^{2+} without any shift in the emission, and the fluorescence is red-shifted (cyan to yellow) in the case of BF_3.

Absorption coefficients were found to be 11 000 cm^{-1} M^{-1} for **SP26**, and for **SP26** with Cu^{2+} and BF_3, they were found to be 6500 and 14 500 cm^{-1} M^{-1}, respectively. The limit of quantification was determined to be as low as 1.27 nM for Cu^{2+} and 1.025 nM for BF_3. The receptor's quantum yield (ϕ_{fl}) was determined to be 0.94, using quinine sulfate as a standard reference (ϕ_{fl} = 0.54). Upon addition of Cu^{2+} and BF_3 to the chemosensor **SP26**, the fluorescence intensity decreases and increases, respectively, with a quantum yield of 0.98 for **SP26** with the BF_3 complex and 0.53 for **SP26** with the Cu^{2+} complex.

2.6 Binding constant and limit of detection

After FL titration, the limit of detection (LoD) of **SP26** towards Cu^{2+} ions and BF_3 was computed utilizing the formula 3σ/slope from the analyte concentration of Cu^{2+} and BF_3 against emission intensity, where σ represents the standard deviation and the slope value is obtained from the linear graph. The results were 381 pM for Cu^{2+} and 307 pM for BF_3 respectively [Fig. 5(a) and (b)]. The Benesi–Hildebrand graph was obtained, illustrating the connection between the

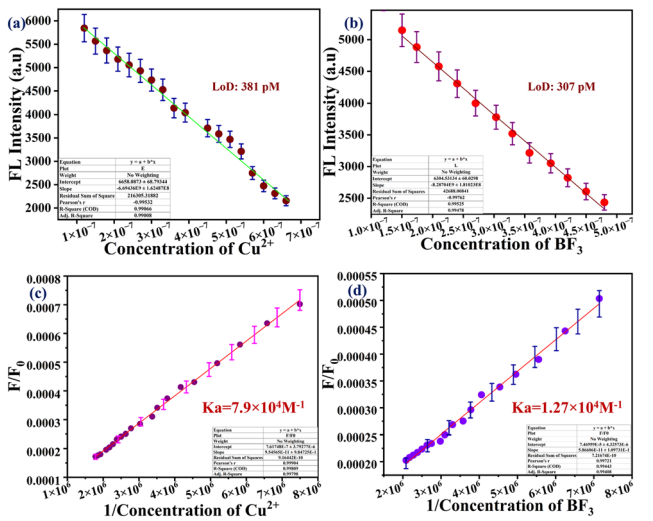

Fig. 5 (a) Calibration plot between the concentration of Cu^{2+} and measured emission intensity. (b) Calibration plot between the concentration of BF_3 and measured emission intensity. (c) Benesi–Hildebrand plot for chemosensor **SP26** with 1/concentration of Cu^{2+} with emission intensity. (d) Benesi–Hildebrand plot for chemosensor **SP26** with 1/concentration of BF_3 with emission intensity.

reciprocal of concentrations of Cu^{2+} and BF_3 against $1/[F - F_0]$ (Fig. 4b). The binding association constants (K_a) for the **SP26 + Cu^{2+}** and **SP26 + BF$_3$** complexes were calculated to be 7.9×10^4 M^{-1} and 1.27×10^4 M^{-1} [Fig. 5(c) and (d)].

2.7 Job's plot, response time studies, and pH studies

In Job's plot analysis (Fig. 6a and b), it is possible to determine the binding ratio of the analyte to chemosensor **SP26**. The 0.5-mole fraction suggests that the binding ratio is 1 : 1 for both **SP26 : Cu^{2+}** and **SP26 : BF$_3$**. Additionally, as shown in Fig. 6c and d, the fluorescence intensity is drastically reduced within a fraction of a second when Cu^{2+} and BF_3 are added to **SP26**. This indicates that the emission intensity decreased immediately, since a complex was generated by **SP26 + Cu^{2+}** and **SP26 + BF$_3$** as soon as analytes are added. The emission spectrum of the chemosensor **SP26** revealed an observable shift in the pH range of 5.0 to 12.0; below 5.0 pH, the emission intensity was high as a result of an increase in the supply of H^+, as seen in Fig. 6e and f. The protonation of nitrogen causes a small increase in emission intensity. Then, the emission intensity varies randomly with pH, influencing the chemosensor **SP26** with Cu^{2+}. The stability at pH 8 up to 12 is observed to some extent. The stability in emission intensity is observed in **SP26** with BF_3 in the pH range of 8.0 up to 12.0. As in the previous case, nitrogen is protonated at lower pH values between 2.0 and 7.0, resulting in the poor complexation of **SP26** with BF_3 lacking a single pair of electrons. Hence, emission intensity changes with different pH on treating **SP26** with BF_3 (Fig. 6f).

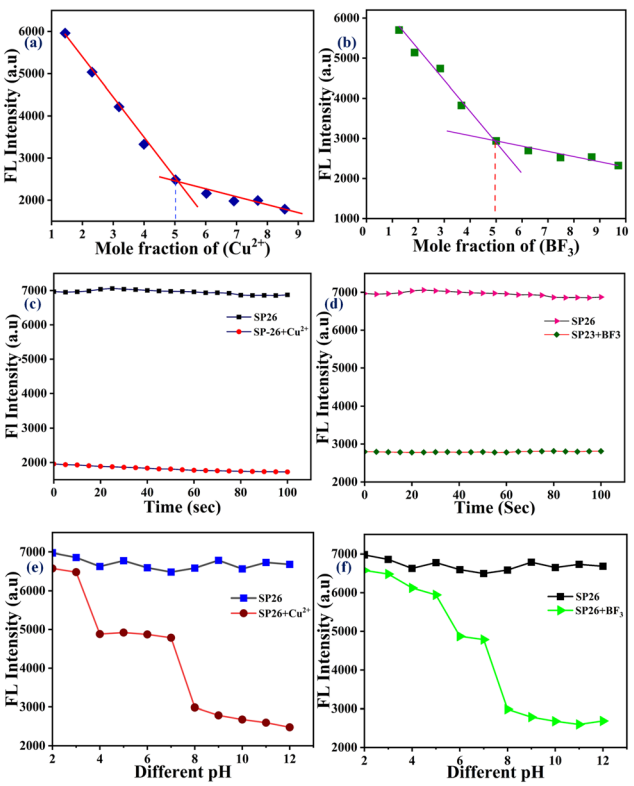

Fig. 6 (a) Job's plot of **SP26** with various mole fractions of Cu^{2+} and emission intensities. (b) Job's plot of **SP26** with various mole fractions of BF_3 and emission intensities. (c) Response time for change in emission intensity after adding Cu^{2+} to **SP26** in 8 : 2 THF : H_2O (2×10^{-5} M). (d) Response time for change in emission intensity after adding BF_3 to **SP26** in 8 : 2 THF : H_2O (2×10^{-5} M); for both, the excitation wavelength is at 360 nm and the emission wavelength is at 500 nm, and the scanned wavelength is 400 to 650 nm at room temperature. (e) The pH effect on the emission intensity of chemosensor **SP26**, and the emission intensity of chemosensor **SP26** with Cu^{2+} pH (2.0–12.0). (f) The pH effect on the emission intensity of chemosensor **SP26**, and the emission intensity of chemosensor **SP26** with BF_3 pH (2.0–12.0).

2.8 Interference studies and reversibility studies

The interference experiments were carried out for chemosensor **SP26**. Along with Cu^{2+} and BF_3, different metal ions and boron species were added separately to chemosensor **SP26**, and there were no changes except for Cu^{2+} and BF_3.

In the case of Cu^{2+} and BF_3, the emission intensity decreases even in the presence of other analytes. This shows the selectivity of chemosensor **SP26** towards Cu^{2+} and BF_3 (Fig. 7(a) and (b)). Additionally, the reversibility of sensor **SP26** was evaluated using EDTA for Cu^{2+} ions. When Cu^{2+} was added to **SP26**, the colour changed from cyan to light blue, and the emission intensity falls (Fig. 7c). The emission intensity increased, and the colour of the **SP26** fluorescence changed from light blue to cyan upon the addition of EDTA. This phenomenon was repeatedly evaluated three times. Similarly, when BF_3 was added to **SP26**, the colour was shifted from cyan to light yellow, and the emission intensity diminished. However, the emission intensity

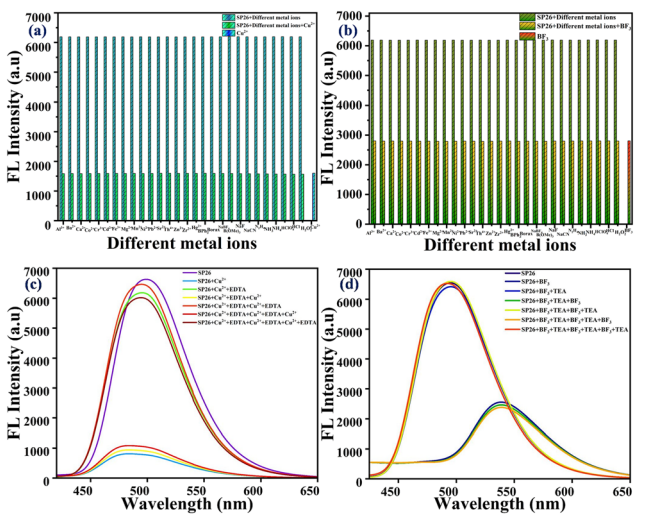

Fig. 7 (a) Interference of other metal ions and boron species (1×10^{-3} M) along with Cu^{2+} on **SP26** in an 8 : 2 THF : H_2O solution (2×10^{-5} M); the excitation wavelength is at 360 nm and the emission wavelength is at 500 nm, and the scanned wavelength is 400 to 650 nm at room temperature. (b) Interference of other metal ions and boron species (1×10^{-3} M) along with BF_3 on **SP26** in an 8 : 2 THF : H_2O (2×10^{-5} M) solution. (c) The reversibility studies of **SP26** in 8 : 2 THF : H_2O (2×10^{-5} M) solution with Cu^{2+} by adding EDTA. (d) The reversibility studies of **SP26** in 8 : 2 THF : H_2O (2×10^{-5} M) solution with BF_3 by adding TEA.

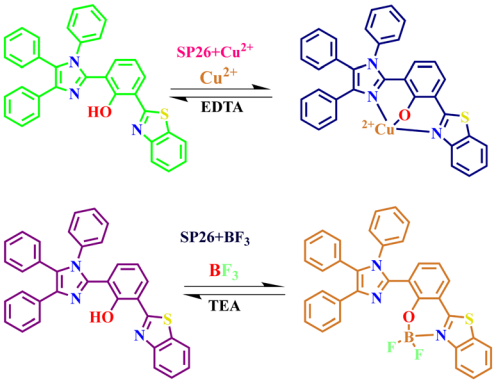

Scheme 2 The mechanism of the reversibility of the chemosensor **SP26** with the addition of Cu^{2+} + EDTA and **SP26** with the addition of BF_3 + TEA.

increases and the color changes back to cyan upon adding triethylamine (TEA) (Fig. 7d). This is due to the formation of a stronger complex between EDTA and Cu^{2+} than between **SP26** and Cu^{2+}. Hence, EDTA replaces **SP26**, and similarly a stronger complex is formed between BF_3 and TEA than between **SP26** and BF_3. Hence, TEA replaces **SP26** (Scheme 2). After this, the chemosensor **SP26** was recovered, and this phenomenon was regularly examined for reproducibility over three cycles.

2.9 Study of the binding mechanism

We have performed ^{1}H NMR for the sensor before and after adding BF_3. Between BF_3 and Cu^{2+}, Cu^{2+} is paramagnetic and hence NMR cannot be recorded. Hence, we have recorded the FT-IR spectrum for the complex, and it has been compared with that of the ligand. By comparing these two, in the spectrum of the complex, the –OH stretching peak at 3400 cm^{-1} completely disappears, and there is a change in the shape of the –C═N stretching peaks at 1300 and 1600 cm^{-1}, indicating that copper forms a complex through oxygen and nitrogen (Fig. 8a).

Binding interactions between **SP26** and BF_3 were studied using ^{1}H NMR titration experiment in DMSO-d_6 and FT-IR. BF_3 binds with the phenolic oxygen when **SP26** is added. In ^{1}H NMR, the –OH proton disappears completely since boron is getting attached to oxygen after removing H^+. Similarly, electrons from the carbon in the benzene ring, next to the nitrogen of benzothiazole, flow to the nitrogen due to the attachment of BF_3. As a result, the peak of the particular proton (H-1) becomes more pronounced and shifted downfield (8.692 ppm). However, all other protons also shifted downfield due to the attachment of BF_3 (8.053, 8.131, 8.169, 8.237 ppm) (Fig. 8c). Also in FT-IR, the –OH peak disappears completely, and there is a change in the shape of the –C═N stretching peaks at 1321 and 1614 cm^{-1}, indicating that boron forms a complex through oxygen and nitrogen (Fig. 8b).

The HR-MS spectrum of **SP26** + **Cu^{2+}** shows a peak at 583.1092 *m*/*z* (Fig. S5), and **SP26** + **BF_3** shows a peak at 570.1635 *m*/*z* (Fig. S6). Utilizing the Gaussian 16W package and

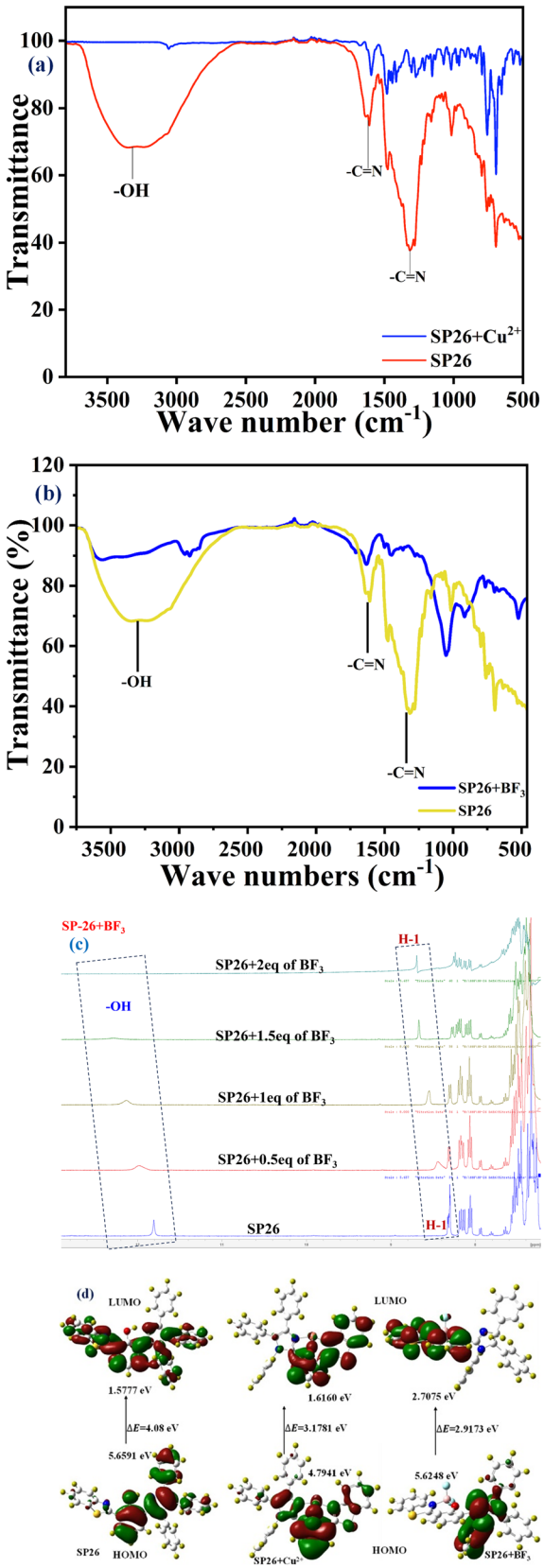

Fig. 8 (a) IR spectra of **SP26** and **SP26** with Cu^{2+}. (b) IR spectra of **SP26** and **SP26** with BF_3. (c) ^{1}H NMR spectra of **SP26** and **SP26** with BF_3 in DMSO-d_6. (d) The optimized structures of the HOMO and LUMO of **SP26** and **SP26** with Cu^{2+} and BF_3 complexes at the DFT/B3LYP analysis.

Table 2 Determination of Cu^{2+} ions in environmental samples

Various water samples	SD (%)	Con. of spiked Cu^{2+} ions (μM)	Con. of the found Cu^{2+} ions (μM)	Recovery of Cu^{2+} added (%)
Tap water	0.458	25	24.85	99.4
Lake water	0.503	25	24.7	98.8
Drinking water	0.529	25	24.85	99.4

theoretical calculations at the B3LYP level with the 6-31'G(d,p) level of theoretical analysis,[46] density functional theory (DFT) was employed to determine the energy of the optimized structures of **SP26** and **SP26** with Cu^{2+} and BF_3 complexes. In **SP26**, the electron density is concentrated in two phenyl groups, one of which is connected to nitrogen in the HOMO. Upon transitioning to a linear molecular orbital LUMO, the electron density disperses across the molecule, sparing all but one phenyl group; as a result, ΔE is 4.08 eV. The HOMO and LUMO of the **SP26 + Cu^{2+}** combination do not differ significantly due to electron spreading. However, the band gap decreases from 4.08 to 3.1781 eV. In the case of the **SP26 + BF$_3$** complex, the difference in electron spreading further decreases (ΔE). As a result, the band gap is further closed to 2.9171 eV. The energy gap suggests that the **SP26 + Cu^{2+}** and BF_3 complexes stabilize the system (Fig. 8c). The chemosensor demonstrates that the interaction of **SP26** with Cu^{2+} and BF_3 affects both twisted intramolecular charge transfer (TICT) and intramolecular charge transfer (ICT).

3. Application in real water samples

Human health suffers significant harm when copper sources contaminate water. The identification of Cu^{2+} ions in environmental samples is therefore essential. Cu^{2+} ion detection was carried out utilizing water samples from several locations across Vellore Institute of Technology, including tap, drinking, and lake water, to track the practical application of sensing probe **SP26**. Chemosensor **SP26** shows high sensitivity and selectivity towards Cu^{2+}. To test how well it can detect Cu^{2+} in real water, we performed a spike and recovery test by checking the brightness of chemosensor **SP26** in tap water, lake water, and drinking water with the addition of Cu^{2+}. All the water samples were centrifuged and filtered before use. The water samples were spiked with a set amount of Cu^{2+} (25 μM). As shown in Table 2, Cu^{2+} was tested in each sample with satisfactory accuracy, which means chemosensor **SP26** could be used for Cu^{2+} detection in water samples. It was discovered that the Cu^{2+} ion concentrations in Cu^{2+} spiked samples agreed fairly well. Further, over 98% of Cu^{2+} was recovered, demonstrating the developed probe's ability to detect Cu^{2+} ions in practice (Table 2).

3.1 Application of chemosensor SP26 in the paper strip test

We created paper strips to detect Cu^{2+} and BF_3 levels, which were simple to use and convenient. The paper strips were created by dipping Whatman filter paper into a solution of 2×10^{-5} M concentration of **SP26**, followed by air drying. Three drops of analyte at a concentration of 1×10^{-3} M were applied to paper strips. We illuminated the strips under a 365 nm UV lamp after allowing them to air dry. Except for Cu^{2+} and BF_3, there was no change in colour. Cu^{2+} produces a colour shift from cyan to light blue. In contrast, BF_3 causes a color change from cyan to yellow (Fig. 9a). The emission color was then gradually altered for both Cu^{2+} and BF_3 (Fig. 9b), as the gradual addition of Cu^{2+} and BF_3 to the paper strips increased from 0 to 3 equivalents and 0 to 2 equivalents, respectively. The results revealed the qualitative detection of Cu^{2+} and BF_3 by the chemosensor **SP26**.

Conclusion

We have synthesized and presented **SP26**, a new imidazole chemosensor characterized by NMR and HRMS analytical techniques. Cu^{2+} quenches emission intensity at 500 nm, and BF_3 reduces emission intensity at 550 nm with a corresponding red shift. The chemosensor **SP26** can be made reversible using EDTA; emission intensity was first quenched by Cu^{2+}, and then it was restored by adding EDTA to **SP26**. Similarly, adding BF_3 to **SP26** caused the emission to move to 550 nm with a reduction in intensity; however, adding TEA to the same solution caused the emission intensity to reversibly change back to **SP26** emission. After that, we studied the binding mechanism using Job's plot, mass spectroscopy, DFT investigations, NMR titration, and FT-IR spectroscopy. For **SP26** with Cu^{2+} and BF_3, a 1 : 1 complex was produced with coordinated imidazole nitrogen and phenolic oxygen atoms. The limit of detection was 381 pM for Cu^{2+} and 307 pM for

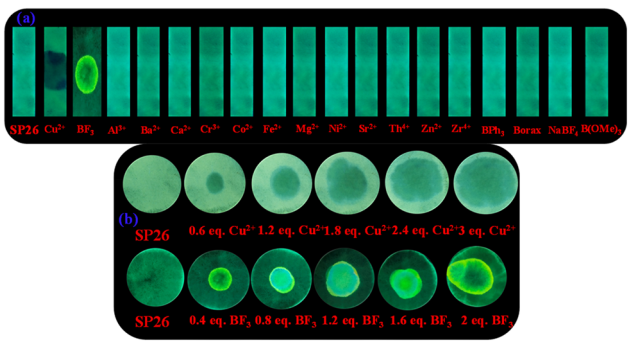

Fig. 9 (a) The photographs exhibiting the emission color change of **SP26** on paper strips, on the addition of different analytes under UV light at 365 nm, and (b) the gradual addition of different equivalents of Cu^{2+} and BF_3 of **SP26**.

BF_3, and the response time was within a second. The rapid qualitative application of paper strip studies and quantitative application in environmental water samples were carried out with our synthesized chemosensor **SP26**.

Conflicts of interest

There are no conflicts to declare.

Data availability

Supplementary information: Copies of $^1H/^{13}C$ $\{^1H\}$ NMR and HRMS spectra for the sensing receptor **SP26** and the **SP26** + **Cu** and $\mathbf{BF_3}$ complexes, along with HRMS spectra and a comparison of results with previous work reported in the literature. See DOI: **https://doi.org/10.1039/D5SD00021A**.

The data supporting this article have been included as part of the SI.

Acknowledgements

Prakash Seenu is grateful to the Vellore Institute of Technology for the Research Associateship, which allows him to receive financial assistance. The DST-FIST NMR facility at VIT is appropriately acknowledged. Dr. R. Srinivasan from SSL, VIT, is acknowledged for language editing.

References

1 T. Shu, Z. Yang, Z. Cen, X. Deng, Y. Deng, C. Dong and Y. Yu, A novel ratiometric fluorescent probe based on a BODIPY derivative for Cu^{2+} detection in aqueous solution, *Anal. Methods*, 2018, **10**, 5755–5762, DOI: **10.1039/C8AY01760C**.

2 E. Gaggelli, H. Kozlowski, D. Valensin and G. Valensin, Copper Homeostasis and Neurodegenerative Disorders (Alzheimer's, Prion, and Parkinson's Diseases and Amyotrophic Lateral Sclerosis), *Chem. Rev.*, 2006, **106**, 1995–2044, DOI: **10.1021/cr040410w**.

3 A. P. S. Gonzáles, M. A. Firmino, C. S. Nomura, F. R. P. Rocha, P. V. Oliveira and I. Gaubeur, Peat as a natural solid-phase for copper preconcentration and determination in a multicommuted flow system coupled to flame atomic absorption spectrometry, *Anal. Chim. Acta*, 2009, **636**, 198204, DOI: **10.1016/j.aca.2009.01.047**.

4 Y. Qiu, J. Li, H. Li, Q. Zhao, H. Wang, H. Fang, D. Fan and W. Wang, A facile and ultrasensitive photoelectrochemical sensor for copper ions using in-situ electrodeposition of cuprous oxide, *Sens. Actuators, B*, 2015, **208**, 485–490, DOI: **10.1016/j.snb.2014.11.061**.

5 P. G. Georgopoulos, A. Roy, M. J. Yonone-Lioy, A. R. E. Opiekun and P. J. Lioy, Environmental copper: its dynamics and human exposure issues, *J. Toxicol. Environ. Health, Part B*, 2001, **4**, 341–394, DOI: **10.1080/109374001753146207**.

6 A. P. S. Gonzáles, M. A. Firmino, C. S. Nomura, F. R. P. Rocha, P. V. Oliveira and I. Gaubeur, Peat as a natural solid-phase for copper preconcentration and determination in a multicommuted flow system coupled to flame atomic absorption spectrometry, *Anal. Chim. Acta*, 2009, **636**, 198–204, DOI: **10.1016/j.aca.2009.01.047**.

7 J. Otero-Romaní, A. Moreda-Piñeiro, A. Bermejo-Barrera and P. Bermejo-Barrera, Evaluation of commercial C18 cartridges for trace elements solid phase extraction from seawater followed by inductively coupled plasma-optical emission spectrometry determination, *Anal. Chim. Acta*, 2005, **536**, 213–218, DOI: **10.1016/j.aca.2004.12.046**.

8 R. Rahil-Khazen, B. J. Bolann, A. Myking and R. J. Ulvik, Multi-element analysis of trace element levels in human autopsy tissues by using inductively coupled atomic emission spectrometry technique (ICP-AES), *J. Trace Elem. Med. Biol.*, 2002, **16**, 15–25, DOI: **10.1016/S0946-672X(02)80004-9**.

9 J. S. Becker, A. Matusch, C. Depboylu, J. Dobrowolska and M. V. Zoriy, Quantitative Imaging of Selenium, Copper, and Zinc in Thin Sections of Biological Tissues (Slugs–Genus Arion) Measured by Laser Ablation Inductively Coupled Plasma Mass Spectrometry, *Anal. Chem.*, 2007, **79**, 6074–6080, DOI: **10.1021/ac0700528**.

10 R. An, D. Zhang, Y. Chen and Y. Cui, A "turn-on" fluorescent and colorimetric sensor for selective detection of Cu^{2+} in aqueous media and living cells, *Sens. Actuators, B*, 2016, **222**, 48–54, DOI: **10.1016/j.snb.2015.08.035**.

11 H. Yu, J.-Y. Lee, S. Angupillai, S. Wang, S. Feng, S. Matsumoto and Y.-A. Son, A new dual fluorogenic and chromogenic "turn-on" chemosensor for Cu^{2+}/F^- ions, *Spectrochim. Acta, Part A*, 2015, **151**, 48–55, DOI: **10.1016/j.saa.2015.06.078**.

12 H. Liu, F. Wu, B. Zhang, C. Tan, Y. Chen, G. Hao, Y. Tan and Y. Jiang, A simple quinoline-derived fluorescent sensor for the selective and sequential detection of copper (II) and sulfide ions and its application in living-cell imaging, *RSC Adv.*, 2016, **6**, 77508–77514, DOI: **10.1039/C6RA15938A**.

13 J. Gao, J. Yin, Z. Tao, Y. Liu, X. Lin, J. Deng and S. Wang, An Ultrasensitive Fluorescence Sensor with Simple Operation for Cu^{2+} Specific Detection in Drinking Water, *ACS Omega*, 2018, **3**, 3045–3050, DOI: **10.1021/acsomega.7b01497**.

14 D. Li, X. Sun, J. Huang, Q. Wang, Y. Feng, M. Chen, X. Meng, M. Zhu and X. Wang, A carbazole-based "turn-on" two-photon fluorescent probe for biological Cu^{2+} detection vis Cu^{2+}-promoted hydrolysis, *Dyes Pigm.*, 2016, **125**, 185–191, DOI: **10.1016/j.dyepig.2015.10.016**.

15 Y. Wang, D. Qiu, M. Li, Y. Liu, H. Chen and H. Li, A new "on-off-on" fluorescent probe containing triarylimidazole chromophore to sequentially detect copper and sulfide ions, *Spectrochim. Acta, Part A*, 2017, **185**, 256–262, DOI: **10.1016/j.saa.2017.05.061**.

16 C. Li, Z. Yang and S. Li, 1,8-Naphthalimide derived dual-functioning fluorescent probe for "turn-off" and ratiometric detection of Cu^{2+} based on two distinct mechanisms in different concentration ranges, *J. Lumin.*, 2018, **198**, 327–336, DOI: **10.1016/j.jlumin.2018.02.031**.

17 S. B. Warrier and P. S. Kharkar, A coumarin-based chemosensor for selective determination of Cu (II) ions based on fluorescence quenching, *J. Lumin.*, 2018, **199**, 407–415, DOI: **10.1016/j.jlumin.2018.03.073**.

18 H. Wang, D.-L. Shi, J. Li, H.-Y. Tang, J. Li and Y. Guo, A facile fluorescent probe with a large Stokes shift for sequentially detecting copper and sulfide in 100% aqueous solution and imaging them in living cells, *Sens. Actuators, B*, 2018, **256**, 600–608, DOI: **10.1016/j.snb.2017.10.124**.

19 Q. Dai, H. Liu, C. Gao, W. Li, C. Zhu, C. Lin, Y. Tan, Z. Yuan and Y. Jiang, A one-step synthesized acridine-based fluorescent chemosensor for selective detection of copper (II) ions and living cell imaging, *New J. Chem.*, 2018, **42**, 613–618, DOI: **10.1039/C7NJ03615A**.

20 X. Shen, H. Zhang and X. He, *et al.*, Evaluating the treatment effectiveness of copper-based algaecides on toxic algae Microcystis aeruginosa using single cell-inductively coupled plasma-mass spectrometry, *Anal. Bioanal. Chem.*, 2019, **411**, 5531–5543, DOI: **10.1007/s00216-019-01933-9**.

21 C. Wu, J. Wang, J. Shen, C. Zhang, Z. Wu and H. Zhou, A colorimetric quinoline-based chemosensor for sequential detection of copper ion and cyanide anions, *Tetrahedron*, 2017, **73**(38), 5715–5719, DOI: **10.1016/j.tet.2017.08.010**.

22 B. Zhang, H. Liu, F. Wu, G. Hao, Y. Chen, C. Tan and Y. Jiang, A dual-response quinoline-based fluorescent sensor for the detection of Copper (II) and Iron (III) ions in aqueous medium, *Sens. Actuators, B*, 2017, **243**, 765–774, DOI: **10.1016/j.snb.2016.12.067**.

23 J. Hu, T. Cao, B. Yuan, Y. Guo, J. Zhang, J. A. Zhao and H. Hou, Benzimidazole-quinoline-based copper complexes: Exploration for their possible antitumor mechanism, *Polyhedron*, 2022, **211**, 115563, DOI: **10.1016/j.poly.2021.115563**.

24 Z. Chen, L. Wang, G. Zou, J. Tang, X. Cai, M. Teng and L. Chen, Highly selective fluorescence turn-on chemosensor based on naphthalimide derivatives for detection of copper (II) ions, *Spectrochim. Acta, Part A*, 2013, **105**, 57–61, DOI: **10.1016/j.saa.2012.12.005**.

25 Y. Ai, Z. Zhu, H. Ding, C. Fan, G. Liu and S. Pu, A dual-responsive fluorescent probe for detection of H2S and Cu^{2+} based on rhodamine-naphthalimide and cell imaging, *J. Photochem. Photobiol., A*, 2022, **427**, 113801, DOI: **10.1016/j.jphotochem.2022.113801**.

26 S. Sun, X. Wu, Y. Huang, Q. Jiang, S. Zhu and S. Sun, Visual detection of Cu^{2+} in high-copper feed based on a fluorescent derivative of rhodamine B, *Microchem. J.*, 2021, **171**, 106858, DOI: **10.1016/j.microc.2021.106858**.

27 E. Karakus, A rhodamine-based fluorescent chemodosimeter for the selective and sensitive detection of copper (II) ions in aqueous media and living cells, *J. Mol. Struct.*, 2021, **1224**, 129037, DOI: **10.1016/j.molstruc.2020.129037**.

28 S. Sarkar, S. Roy, A. Sikdar, R. N. Saha and S. S. Panja, A pyrene-based simple but highly selective fluorescence sensor for Cu^{2+} ions via a static excimer mechanism, *Analyst*, 2013, **138**(23), 7119–7126, DOI: **10.1039/C3AN00928A**.

29 M. Huang, L. Hu, H. Shen, Q. Liu, M. I. Hussain, J. Pan and Y. Xiong, Sulfination of alcohols with sodium sulfinates promoted by $BF_3{\cdot}OEt_2$: an unexpected access, *Green Chem.*, 2016, **18**, 1874–1879, DOI: **10.1039/C5GC02846A**.

30 S. M. Vijayan, T. Göen, K. Dennerlein, R. E. Horch, I. Ludolph, H. Drexler and S. Kilo, Calcium, magnesium and aluminium ions as decontaminating agents against dermal fluoride absorption following hydrofluoric acid exposure, *Toxicol. In Vitro*, 2021, **71**, 105055, DOI: **10.1016/j.tiv.2020.105055**.

31 Y. Liu, J. Zhang, Y. Wang, C. Liu, G. Zhang and W. Liu, A rapid and naked-eye visible FRET ratiometric fluorescent chemosensor for sensitive detection of toxic BF_3, *Sens. Actuators, B*, 2017, **243**, 940–945, DOI: **10.1016/j.snb.2016.12.078**.

32 L. T. White, *Hazardous Gas Monitoring, Fifth Edition, A guide for Semiconductor and Other Hazardous Occupancies*, 2025.

33 P. Banet, L. Legagneux, P. Hesemann, J. Moreau, L. Nicole, A. Quach, C. Sanchez and T. Tran-Thi, Hybrid mesostructured thin films functionalized with DBM as new selective sensors of BF_3, *Sens. Actuators, B*, 2008, **130**, 1–8, DOI: **10.1016/j.snb.2007.07.103**.

34 C.-K. Koo, F. Samain, N. Dai and E. T. Kool, DNA polyfluorophores as highly diverse chemosensors of toxic gases, *Chem. Sci.*, 2011, **2**, 1910, DOI: **10.1039/c1sc00301a**.

35 K. Dhanunjayarao, V. Mukundam, R. V. R. N. Chinta and K. Venkatasubbaiah, Synthesis of highly fluorescent imidazole-based diboron complex, *J. Organomet. Chem.*, 2018, **865**, 234–238, DOI: **10.1016/j.jorganchem.2018.04.026**.

36 V. Mukundam, K. Dhanunjayarao, C. N. Chuang, D. Y. Kang, M. K. Leung, K. H. Hsieh and K. Venkatasubbaiah, Design, synthesis, photophysical and electrochemical properties of 2-(4, 5-diphenyl-1-p-aryl-1 H-imidazol-2-yl) phenol-based boron complexes, *Dalton Trans.*, 2015, **44**(22), 10228–10236, DOI: **10.1039/C5DT00867K**.

37 G. Prabakaran, K. Velmurugan, R. Vickram, C. I. David, A. Thamilselvan, J. Prabhu and R. Nandhakumar, Triphenyl-imidazole-based reversible colorimetric/fluorimetric sensing and electrochemical removal of Cu^{2+} ions using capacitive deionization and molecular logic gates, *Spectrochim. Acta, Part A*, 2021, **246**, 119018, DOI: **10.1016/j.saa.2020.119018**.

38 M. H. Mahnashi, A. M. Mahmoud, S. A. Alkahtani, R. Ali and M. M. El-Wekil, A novel imidazole-derived colorimetric and fluorometric chemosensor for bifunctional detection of copper (II) and sulphide ions in environmental water samples, *Spectrochim. Acta, Part A*, 2020, **228**, 117846, DOI: **10.1016/j.saa.2019.117846**.

39 A. Da Lama, J. P. Sestelo, L. Valencia, D. Esteban-Gómez, L. A. Sarandeses and M. M. Martínez, Synthesis and structural analysis of push-pull imidazole-triazole-based fluorescent bifunctional chemosensor for Cu^{2+} and Fe^{2+} detection, *Dyes Pigm.*, 2022, **205**, 110539, DOI: **10.1016/j.dyepig.2022.110539**.

40 S. M. Kumar, S. Munusamy, D. Jothi, S. Enbanathan and S. K. I. Iyer, Rationally constructed imidazole derivatized Schiff-base based fluorescent sensor for reversible identification of copper ions and its applications in fingerprint imaging, *J. Mol. Liq.*, 2023, **373**, 121235, DOI: **10.1016/j.molliq.2023.121235**.

41 S. Manoj Kumar and S. Kulathu Iyer, D–π–A–π–D-Configured Imidazole-Tethered Benzothiadiazole-Based Sensor for the Ratiometric Discrimination of Picric Acid: Applications in Latent Fingerprint Imaging, *J. Org. Chem.*, 2024, **89**(8), 5392–5400, DOI: **10.1021/acs.joc.3c02803**.

42 C. Bathula, M. K. Ravindra, K. Ashok Kumar, H. Yadav, S. Ramesh, S. Shinde, N. K. Shrestha, K. M. Mahadevan, V. Reddy and A. Mohammed, Microwave assisted synthesis of imidazolyl fluorescent dyes as antimicrobial agents, *J. Mater. Res. Technol.*, 2020, **9**, 6900–6908, DOI: **10.1016/j.jmrt.2020.01.011**.

43 W. A. Ahmed Arafa, An eco-compatible pathway to the synthesis of mono and bis-multi substituted imidazole's over novel reusable ionic liquids: an efficient and green sonochemical process, *RSC Adv.*, 2018, **8**, 16392–16399, DOI: **10.1039/C8RA02755B**.

44 S. A. Shahzad, T. Javid, M. A. Assiri, A. Pervaiz, H. Irshad, F. S. Han and D. D. He, Drug molecules beyond chemical biology: fluorescence and DFT-based investigations for fluoride ion sensing and the trace detection of chloroform, *RSC Adv.*, 2024, **14**(51), 3799338001, DOI: **10.1039/D4RA04844J**.

45 A. Shabbir, S. A. Shahzad, A. Y. A. Alzahrani, Z. A. Khan, M. Yar and W. Rauf, A Multimode fluorescent sensor for sequential detection of Cu^{2+} and cysteine as well as pH sensor with real sample Applications: Extensive experimental and DFT studies, *Spectrochim. Acta, Part A*, 2025, **327**, 125414, DOI: **10.1016/j.saa.2024.125414**.

46 C. Adamo and D. Jacquemin, The calculations of excited-state properties with Time-Dependent Density Functional Theory, *Chem. Soc. Rev.*, 2013, **42**, 845–856, DOI: **10.1039/C2CS35394F**.